

A Fast Volume Integral Equation Solver with Linear Basis Functions for the Accurate Computation of Electromagnetic Fields in MRI

Ioannis P. Georgakis, Ilias I. Giannakopoulos, Mikhail S. Litsarev,
and Athanasios G. Polimeridis, *Senior Member, IEEE*

Abstract—Objective: This paper proposes a stable volume integral equation (VIE) solver based on polarization/magnetization currents, for the accurate and efficient computation of the electromagnetic scattering from highly inhomogeneous and high contrast objects. **Methods:** We employ the Galerkin Method of Moments to discretize the formulation with discontinuous piecewise linear basis functions on uniform voxelized grids, allowing for the acceleration of the associated matrix-vector products in an iterative solver, with the help of FFT. **Results:** Numerical experiments are conducted to study the accuracy and convergence properties of the proposed framework. Their results are compared against standard low order (piecewise constant) discretization schemes, a more conventional VIE formulation based on electric flux densities, and a commercial software package that employs the finite difference time domain method. **Conclusion:** The results illustrate the superior accuracy and well-conditioned properties of the proposed scheme. **Significance:** The developed solver can be applied to accurately analyze complex geometries, including realistic human body models, typically used in modeling the interactions between electromagnetic waves and biological tissue, that arise in magnetic resonance scanners.

Index terms— Electromagnetic scattering, high contrast/inhomogeneity, high-order basis functions, magnetic resonance modeling, method of moments, volume integral equations.

I. INTRODUCTION

Numerical modeling of electromagnetic (EM) scattering from extremely inhomogeneous objects and objects with high contrast is of great interest. Over the last decades, a plethora of numerical algorithms and computational methods has been developed for applications in wireless communications, microwave instrumentation, and remote sensing. However, more challenging problems arise, such as modeling the interactions between EM waves and biological tissue, which is of great relevance for the determination of the deposited radio-frequency (RF) power inside the human body and the associated safety considerations at high-field magnetic resonance imaging (MRI). Specifically, at high and ultra-high magnetic field strengths, the operating frequency of the associated RF coils also increases. Hence, the wavelength becomes comparable to or even smaller than the effective dimension of

the human body, potentially increasing the specific absorption rate (SAR) and deteriorating the magnetic field homogeneity and thus the image quality. Therefore, the accurate estimation of the local distribution of the EM fields, generated by an external RF source, as well as the absorbed power, described by SAR, calls for the implementation of novel and more efficient electrodynamic solvers, to achieve a reliable numerical solution. Developing such precise simulation tools poses a great challenge since from a computational EM perspective the human body is highly inhomogeneous and presents great geometrical complexity.

Regarding the numerical techniques for computing the EM fields in inhomogeneous dielectrics, such as the human body, there is a vast amount of literature and a rich investigative activity. On one hand, there are methods based on the partial differential form of Maxwell equations, such as the finite differences (FD) and finite element (FE) method, which are known for their generality and versatility in many application areas. On the other hand, there are methods that start from Maxwell equations in their integro-differential form, such as the integral equation (IE) methods, which offer great flexibility in exploiting certain problem properties by customization of the method. IE methods, despite being complicated and computationally expensive, have proven to be the method of choice for modeling inhomogeneous objects by dividing the arbitrary scatterer into simple volumetric tessellations, with piecewise homogeneous properties. Furthermore, a volume integral equation (VIE)-based solver can be effortlessly embedded into a surface integral equation (SIE) solver to calculate the EM field distributions and RF transmit and receive coils interactions in the presence of realistic human body models (RHBMs) [1]. However, the development of an efficient and stable numerical EM simulation software based on integral equations is far from being a trivial task. Towards that direction, there has been a recent contribution [2], where a stable current-based VIE solver with piecewise constant (PWC) basis functions has been developed and incorporated into [3] for the fast EM analysis of MR coils.

In the MR modeling case, there is an internal limitation with respect to the spatial resolution and thus the grid refinements in a numerical solver. This naturally leads to the exploitation of p -refinement techniques for achieving more reliable solutions in a VIE-based solver, too. In this work, we modify the aforementioned current-based VIE solver [2] and equip it with higher-order basis functions, that yield more accurate

This work was supported by grants from the Skoltech-MIT Next Generation Program. (Corresponding author: Ioannis P. Georgakis.)

Ioannis P. Georgakis, Ilias I. Giannakopoulos and Mikhail S. Litsarev are with the Skoltech Center for Computational Data-Intensive Science and Engineering, Skolkovo Institute of Science and Technology, 121205 Moscow, Russia (e-mail: ioannis.georgakis@skolkovotech.ru).

Athanasios G. Polimeridis is with Q Bio, Redwood, CA 94063, USA.

results for modeling highly inhomogeneous and high contrast objects, without the need of refining the mesh. Namely, discontinuous piecewise linear (PWL) [4], [5] basis and testing functions are utilized and defined with support a single voxel of a uniform grid that allows for the fast calculation of the associated matrix-vector products with the help of FFT, exploiting the block Toeplitz structure of the system's matrix, since the arising integral kernels are translationally invariant. Plenty of research studies exist in the literature regarding this problem [6]–[30]. Furthermore, the aforementioned currents must not necessarily satisfy any continuity conditions between neighboring elements, voxels in our case, allowing for the use of testing and basis functions that span L^2 , when employing Method of Moments (MoM). This way, the finite-energy conditions are respected and the spectral properties of the operators are preserved, as it has been shown in recent studies [31], [32]. Moreover, the resulting formulation calls for the numerical integration of singular volume-volume Galerkin inner products, but as it has been shown in previous work [33]–[36], there exist readily available formulas that reduce both the dimensionality and singularity order of the kernels, allowing for the fast and precise numerical evaluation of the singular integrals by means of well-established sophisticated cubatures [37]–[43], originally developed for SIE formulations. Recent contributions have also expanded the analysis for arbitrary quadrilateral patches [44], [45].

Finally, through numerical experiments, we illustrate that the resulting discretized formulation is well-conditioned and has superior convergence properties than the discretized version with PWC approximations and than a more standard VIE formulation based on electric flux densities [30]. Specifically, the number of iterations of the iterative solver remains practically the same as with the case of PWC basis functions and is much smaller than that of the flux-based solver, for highly inhomogeneous scatterers. Another favorable feature of the proposed scheme is its superior accuracy. To demonstrate that, we present a comparative analysis between the PWC and the PWL basis solver for a homogeneous sphere, comparing both solvers with analytical results obtained with Mie series [46], and for RHBMs from the Virtual Family Population [47]. Even when numerically treating the case of dielectric shimming [48], where high-permittivity dielectric pads are placed in the vicinity of a RHBM, the suggested work performs effectively. However, naturally, this comes with an increase in the computational cost and in the required memory footprint. Thankfully, the arising Green function tensors in FFT-based VIEs preserve low multilinear rank properties [49], [50], thus, we can overcome this limiting factor and accelerate the solution of the linear system of equations by combining tensor decompositions and parallel programming techniques of graphical processing units (GPUs) [51].

The remainder of the paper is organized as follows. In Section II, we set up the current-based VIE formulation and describe its superior properties in comparison with other VIE formulations. In Section III, we introduce the novel discretization scheme with PWL basis functions, formulate the linear system by means of MoM, and represent the system in a tensor format for a better comprehension. In Section IV, we

describe the procedure to accelerate the matrix-vector product and develop a fast FFT-based solver. Finally, in Section V, we validate the proposed solver by comparison with the analytical solution for spheres and demonstrate its accuracy and convergence properties when modeling the EM scattering from RHBMs.

TABLE I
NOTATION

Notation	Description
i	imaginary unit
a	scalar in \mathbb{C}
\mathbf{a}	vector in \mathbb{C}^3 , $\mathbf{a} = (a_x, a_y, a_z)$
\mathbf{a}	1-D array, vector in \mathbb{C}^N
\mathbf{A}	2-D array, matrix in $\mathbb{C}^{N_1 \times N_2}$
$\underline{\mathbf{A}}$	m -D array, tensor in $\mathbb{C}^{N_1 \times N_2 \times \dots \times N_m}$
\mathcal{A}/\mathcal{A}	continuous operator acting in $\mathbb{C}^3/\mathbb{C}^6$
\odot	element-wise multiplication

II. VOLUME INTEGRAL EQUATION FORMULATION

We consider the scattering of time-harmonic EM waves by a penetrable object, occupying the bounded domain Ω in 3-D Euclidean space, \mathbb{R}^3 . The working angular frequency is $\omega \in \mathbb{R}^+$ and the electric properties are defined as

$$\begin{aligned} \epsilon &= \epsilon_0, & \mu &= \mu_0 & \text{in } \mathbb{R}^3 \setminus \Omega, \\ \epsilon &= \epsilon_r(\mathbf{r})\epsilon_0, & \mu &= \mu_r(\mathbf{r})\mu_0 & \text{in } \Omega. \end{aligned} \quad (1)$$

Here, the vacuum (or free-space) permittivity ϵ_0 and permeability μ_0 are real positive values, and the relative permittivities $\epsilon_r(\mathbf{r})$ and $\mu_r(\mathbf{r})$ are assumed complex:

$$\begin{aligned} \epsilon_r(\mathbf{r}) &= \epsilon'_r(\mathbf{r}) - i\epsilon''_r(\mathbf{r}), \\ \mu_r(\mathbf{r}) &= \mu'_r(\mathbf{r}) - i\mu''_r(\mathbf{r}), \end{aligned} \quad (2)$$

with $\epsilon'_r, \mu'_r \in (0, \infty)$ and $\epsilon''_r, \mu''_r \in [0, \infty)$, assuming a time factor $\exp(i\omega t)$. At this point, we also define the free space wave number, $k_0 = \omega\sqrt{\mu_0\epsilon_0}$.

The total time harmonic fields (\mathbf{e}, \mathbf{h}) in the presence of an isotropic and inhomogeneous object can be decomposed into incident $(\mathbf{e}_{\text{inc}}, \mathbf{h}_{\text{inc}})$ and scattered $(\mathbf{e}_{\text{sca}}, \mathbf{h}_{\text{sca}})$ fields:

$$\begin{pmatrix} \mathbf{e} \\ \mathbf{h} \end{pmatrix} = \begin{pmatrix} \mathbf{e}_{\text{inc}} \\ \mathbf{h}_{\text{inc}} \end{pmatrix} + \begin{pmatrix} \mathbf{e}_{\text{sca}} \\ \mathbf{h}_{\text{sca}} \end{pmatrix}, \quad (3)$$

where the incident fields are the fields generated by the impressed currents or the sources in the absence of the scatterer and the scattered fields are given by the induced currents due to the presence of the scatterer, as in [2], [22]:

$$\begin{pmatrix} \mathbf{e}_{\text{sca}} \\ \mathbf{h}_{\text{sca}} \end{pmatrix} = \begin{pmatrix} \frac{1}{c_e} \mathcal{L} & -\mathcal{K} \\ \mathcal{K} & \frac{1}{c_m} \mathcal{L} \end{pmatrix} \begin{pmatrix} \mathbf{j} \\ \mathbf{m} \end{pmatrix}, \quad (4)$$

where the equivalent polarization and magnetization currents are defined as

$$\begin{aligned} \mathbf{j}(\mathbf{r}) &\triangleq c_e \chi_e(\mathbf{r}) \mathbf{e}(\mathbf{r}), \\ \mathbf{m}(\mathbf{r}) &\triangleq c_m \chi_m(\mathbf{r}) \mathbf{h}(\mathbf{r}), \end{aligned} \quad (5)$$

with $c_e, c_m \triangleq i\omega\epsilon_0, i\omega\mu_0$ and the electric and magnetic susceptibilities are respectively given by

$$\begin{aligned}\chi_e &\triangleq \epsilon_r - 1, \\ \chi_m &\triangleq \mu_r - 1.\end{aligned}\quad (6)$$

More explicitly, the associated continuous integro-differential operators are:

$$\mathcal{L}\mathbf{u} \triangleq (k_0^2 + \nabla\nabla\cdot)\mathcal{S}(\mathbf{u}; \Omega)(\mathbf{r}), \quad (7a)$$

$$\mathcal{K}\mathbf{u} \triangleq \nabla \times \mathcal{S}(\mathbf{u}; \Omega)(\mathbf{r}), \quad (7b)$$

where

$$\mathcal{S}(\mathbf{u}; \Omega)(\mathbf{r}) \triangleq \int_{\Omega} g(\mathbf{r} - \mathbf{r}')\mathbf{u}(\mathbf{r}')d\mathbf{r}' \quad (8)$$

and g is the free-space scalar Green function:

$$g(\mathbf{r}) = \frac{e^{-ik_0|\mathbf{r}|}}{4\pi|\mathbf{r}|}. \quad (9)$$

Next, making use of the following identity [13]:

$$\mathcal{L}\mathbf{u} = \mathcal{N}\mathbf{u} - \mathbf{u}, \quad (10)$$

where

$$\mathcal{N}\mathbf{u} \triangleq \nabla \times \nabla \times \mathcal{S}(\mathbf{u}; \Omega)(\mathbf{r}), \quad (11)$$

we can rewrite the integro-differential operators, that map the electric and magnetic currents to electric and magnetic fields, in a more computationally friendly form:

$$\begin{pmatrix} \mathbf{e}_{\text{sca}} \\ \mathbf{h}_{\text{sca}} \end{pmatrix} = \underbrace{\begin{pmatrix} \frac{1}{c_e}(\mathcal{N} - \mathcal{I}) & -\mathcal{K} \\ \mathcal{K} & \frac{1}{c_m}(\mathcal{N} - \mathcal{I}) \end{pmatrix}}_{\mathcal{G}} \begin{pmatrix} \mathbf{j} \\ \mathbf{m} \end{pmatrix}. \quad (12)$$

Finally, we derive the current-based volume integral equation for polarization and magnetization currents by combining (3), (5), and (12), as in [52]:

$$\mathcal{A} \begin{pmatrix} \mathbf{j} \\ \mathbf{m} \end{pmatrix} = \mathcal{C}\mathcal{M}_{\chi} \begin{pmatrix} \mathbf{e}_{\text{inc}} \\ \mathbf{h}_{\text{inc}} \end{pmatrix}, \quad (13)$$

where

$$\mathcal{A} = \begin{pmatrix} \mathcal{M}_{\epsilon_r} - \mathcal{M}_{\chi_e}\mathcal{N} & c_e\mathcal{M}_{\chi_e}\mathcal{K} \\ -c_m\mathcal{M}_{\chi_m}\mathcal{K} & \mathcal{M}_{\mu_r} - \mathcal{M}_{\chi_m}\mathcal{N} \end{pmatrix}, \quad (14a)$$

$$\mathcal{C} = \begin{pmatrix} c_e\mathcal{I} & 0 \\ 0 & c_m\mathcal{I} \end{pmatrix}, \quad (14b)$$

$$\mathcal{M}_{\chi} = \begin{pmatrix} \mathcal{M}_{\chi_e} & 0 \\ 0 & \mathcal{M}_{\chi_m} \end{pmatrix}. \quad (14c)$$

\mathcal{M}_{ϕ} is a multiplication operator that multiplies with the function ϕ and \mathcal{I} is the identity dyadic tensor. The focal point of this work revolves around the interaction between EM waves and biological tissue, which can be considered as purely dielectric, and (13) reduces to the following:

$$(\mathcal{M}_{\epsilon_r} - \mathcal{M}_{\chi_e}\mathcal{N})\mathbf{j} = c_e\mathcal{M}_{\chi_e}\mathbf{e}_{\text{inc}}, \quad (15)$$

and the electric and magnetic field in the scatterer can be calculated as

$$\mathbf{e}_{\text{tot}} = \mathbf{e}_{\text{inc}} + \frac{1}{c_e}(\mathcal{N} - \mathcal{I})\mathbf{j}, \quad (16a)$$

$$\mathbf{h}_{\text{tot}} = \mathbf{h}_{\text{inc}} + \mathcal{K}\mathbf{j}. \quad (16b)$$

III. DISCRETIZATION SCHEME

As demonstrated in recent studies, the current-based formulation has superior spectral properties when compared with the other alternatives, i.e., flux- and field-based formulations [2], [22], [31], [32]. In order to achieve this superior performance and guarantee convergence in the norm of the solution, when employing a Galerkin projection method, the function space of the basis and testing functions should be carefully chosen [53], [54]. Specifically, the testing functions should span the L^2 dual of the range space of the associated operator. In our case, as we describe in the next section, the basis functions do not have to enforce any continuity across the interfaces of the discretization elements, so the natural function space of choice is that of square integrable functions $L^2(\mathbb{R}^3)$. Also, it is worth noting that the mapping properties of the current-based formulation, as expressed in (13), are given by

$$L^2(\mathbb{R}^3) \rightarrow L^2(\mathbb{R}^3). \quad (17)$$

All these prerequisites are in accordance with previous work for a current-based VIE with PWC basis functions [2]. However, the nature of the application at hand often requires higher accuracy, especially by means of p -refinement, i.e., using higher-order approximation of the VIE's unknown.

A. Piecewise Linear Basis Functions on Voxels

We begin our analysis by defining the computation domain and the associated discretization grid. We use a rectangular parallelepiped that encloses the inhomogeneous scatterer but does not have to extend any farther than that, since the radiation conditions at infinity are satisfied by the Green function. By denoting the dimensions of this rectangular box as L_x, L_y and L_z , we can now discretize it with $N_V = N_x \times N_y \times N_z$ number of voxels, which in the general case may be non-uniform and have side length $\Delta x = L_x/N_x, \Delta y = L_y/N_y$, and $\Delta z = L_z/N_z$. Having defined the grid, we expand the unknown equivalent polarization and magnetization currents in terms of suitable vector basis functions. These currents are unlikely to satisfy any continuity conditions because of the material discontinuities and as a result the function space of choice in a Galerkin discretization scheme should be $[L^2(\mathbb{R}^3)]^3$. Without loss of generality, we proceed in the following with the expansion only for the polarization currents, since for the magnetization currents the basis functions would be identical,

$$\mathbf{j}(\mathbf{r}) = j_x(\mathbf{r})\hat{\mathbf{x}} + j_y(\mathbf{r})\hat{\mathbf{y}} + j_z(\mathbf{r})\hat{\mathbf{z}}, \quad (18)$$

where each component of the current can be expanded in some discrete set of appropriate basis functions. In this work, we utilize the PWL basis functions, hence the current approximation reads

$$j_q(\mathbf{r}) \approx \sum_{\mathbf{n}=(1,1,1)}^{(N_x, N_y, N_z)} \sum_{l=1}^4 N_{\mathbf{n}}^l(\mathbf{r})a_{\mathbf{n}}^{ql}, \quad (19)$$

where $q \in \{x, y, z\}$ indicates the components of the current, $\mathbf{n} = n_x\hat{\mathbf{x}} + n_y\hat{\mathbf{y}} + n_z\hat{\mathbf{z}}$ is a compound index denoting the centers of the voxels in the grid, $N_{\mathbf{n}}^l(\mathbf{r})$ are the 4 basis functions per current component per voxel, and $a_{\mathbf{n}}^{ql}$ are the

unknown coefficients. In detail, the scalar basis functions are defined as

$$N_n^1(\mathbf{r}) = P_n(\mathbf{r}), \quad (20a)$$

$$N_n^2(\mathbf{r}) = \frac{x - x_n}{\Delta x} P_n(\mathbf{r}), \quad (20b)$$

$$N_n^3(\mathbf{r}) = \frac{y - y_n}{\Delta y} P_n(\mathbf{r}), \quad (20c)$$

$$N_n^4(\mathbf{r}) = \frac{z - z_n}{\Delta z} P_n(\mathbf{r}), \quad (20d)$$

where $\mathbf{r}_n = (x_n, y_n, z_n)$ is the center of each voxel, $P_n(\mathbf{r})$ is a volumetric pulse which is equal to 1 inside voxel \mathbf{n} and 0 otherwise. From the above, it follows that the PWL basis functions have support a single element (voxel in our case) of the grid allowing for discontinuities between neighboring voxels. The vector-valued basis function at voxel \mathbf{n} is:

$$\mathbf{f}_n(\mathbf{r}) = \sum_{q \in \{x, y, z\}} \sum_{l=1}^4 \mathbf{f}_n^{ql}(\mathbf{r}), \quad (21a)$$

$$\mathbf{f}_n^{ql}(\mathbf{r}) = N_n^l(\mathbf{r}) \hat{\mathbf{q}}, \quad (21b)$$

resulting in 12 unknowns per voxel. Finally, the electric properties of the scatterer are modeled by means of PWC approximations:

$$\epsilon_r(\mathbf{r}) \approx \sum_{\mathbf{n}=(1,1,1)}^{(N_x, N_y, N_z)} \epsilon_r(\mathbf{r}_n) P_n(\mathbf{r}). \quad (22)$$

B. Galerkin Inner Products and Linear System Formalism

In what follows, we describe the required steps to numerically solve the current-based formulation of (15) by means of Galerkin MoM, where the equivalent volumetric currents are expanded in the vector-valued square-integrable basis function (21) and tested with the same function. At this point, we can form the linear system $\mathbf{A}\mathbf{x} = \mathbf{b}$ with $\mathbf{x}, \mathbf{b} \in \mathbb{C}^N$ and $\mathbf{A} \in \mathbb{C}^{N \times N}$ with $N = 12N_V$. More specifically, the matrix and the right-hand-side are given by

$$\mathbf{A} = \mathbf{M}_{\epsilon_r} \mathbf{G} - \mathbf{M}_{\chi_e} \mathbf{N}, \quad (23a)$$

$$\mathbf{b} = c_e \mathbf{M}_{\chi_e} \mathbf{e}_{\text{inc}}, \quad (23b)$$

with

$$\mathbf{N} = \langle \mathbf{f}_m^{pl}(\mathbf{r}), \mathcal{N} \mathbf{f}_n^{ql'}(\mathbf{r}) \rangle_{V_m}, \quad (24a)$$

$$\mathbf{K} = \langle \mathbf{f}_m^{pl}(\mathbf{r}), \mathcal{K} \mathbf{f}_n^{ql'}(\mathbf{r}) \rangle_{V_m}, \quad (24b)$$

where $p, q \in \{x, y, z\}$, $l, l' \in \{1, 2, 3, 4\}$, $\mathbf{m} = m_x \hat{\mathbf{x}} + m_y \hat{\mathbf{y}} + m_z \hat{\mathbf{z}}$ denotes the observation voxel and \mathbf{n} the source voxel. Each voxel interacts with each other so $n_x, m_x = 1 : N_x$, $n_y, m_y = 1 : N_y$ and $n_z, m_z = 1 : N_z$ resulting in the dense matrices $\mathbf{N}, \mathbf{K} \in \mathbb{C}^{N \times N}$, where \mathcal{K} operator is discretized for the computation of the magnetic field, too. Furthermore, $\mathbf{G} \in \mathbb{R}^{N \times N}$ is the associated Gram matrix, which is diagonal, since non-overlapping basis functions are used:

$$\mathbf{G} = \langle \mathbf{f}_m^{pl}(\mathbf{r}), \mathbf{f}_n^{ql'}(\mathbf{r}) \rangle_{V_m}. \quad (25)$$

Also, $\mathbf{M}_{\epsilon_r}, \mathbf{M}_{\chi_e} \in \mathbb{C}^{N \times N}$ are diagonal matrices for isotropic materials with the non-zero values being equal to the material

properties at the corresponding voxels. Finally, the "tested" incident electric field that arises from the right-hand-side is given by

$$\mathbf{e}_{\text{inc}} = \langle \mathbf{f}_m^{pl}(\mathbf{r}), \mathbf{e}_{\text{inc}}(\mathbf{r}) \rangle_{V_m}. \quad (26)$$

In the above equations, we use the following definition for the inner products:

$$\langle \mathbf{f}, \mathbf{g} \rangle_V = \int_V \bar{\mathbf{f}} \cdot \mathbf{g} dV, \quad (27)$$

where the $\bar{\cdot}$ denotes the complex conjugate operation.

C. Tensor Representation of the Linear System

The various components of the VIE linear system admit a convenient and intuitive representation in tensor format (multi-dimensional arrays) when we employ a uniform discretization grid. First, we construct the tensors of the dielectric properties of the scatterer, $\underline{\mathbf{M}}_{\epsilon_r}, \underline{\mathbf{M}}_{\chi_e} \in \mathbb{C}^{N_x \times N_y \times N_z}$, as follows:

$$\underline{\mathbf{M}}_{\epsilon_r}(\mathbf{m}) = \epsilon_r(\mathbf{r}_m), \quad (28a)$$

$$\underline{\mathbf{M}}_{\chi_e}(\mathbf{m}) = \epsilon_r(\mathbf{r}_m) - 1. \quad (28b)$$

Next, we form the tensor of the unknowns, $\underline{\mathbf{x}}^{pl} \in \mathbb{C}^{N_x \times N_y \times N_z}$, where $p \in \{x, y, z\}$ and $l \in \{1, 2, 3, 4\}$. Similarly, we construct the tensor of the incident fields. More specifically, the associated tensor of the component p and the scalar basis function l reads

$$\underline{\mathbf{e}}_{\text{inc}}^{pl}(\mathbf{m}) = \int_{V_m} \mathbf{f}_m^{pl}(\mathbf{r}) \cdot \mathbf{e}_{\text{inc}}(\mathbf{r}) dV = \int_{V_m} N_m^l(\mathbf{r}) e_{\text{inc}}^p(\mathbf{r}) dV, \quad (29)$$

resulting in $\underline{\mathbf{e}}_{\text{inc}}^{pl} \in \mathbb{C}^{N_x \times N_y \times N_z}$. Naturally, the tensor of the right-hand-side is given by

$$\underline{\mathbf{b}}^{pl}(\mathbf{m}) = c_e \underline{\mathbf{M}}_{\chi_e} \odot \underline{\mathbf{e}}_{\text{inc}}^{pl}. \quad (30)$$

In order to calculate the interactions between the testing and basis functions, we have to calculate the integrals:

$$\underline{\mathbf{G}}_{m,n}^{pl,ql'} = \int_{V_m} \mathbf{f}_m^{pl} \cdot \mathbf{f}_n^{ql'} dV = \hat{\mathbf{p}} \cdot \hat{\mathbf{q}} \int_{V_m} N_m^l N_n^{l'} dV \quad (31)$$

for $n_x, m_x = 1 : N_x$, $n_y, m_y = 1 : N_y$ and $n_z, m_z = 1 : N_z$, $p, q \in \{x, y, z\}$ and $l, l' \in \{1, 2, 3, 4\}$ which can be uniquely expressed by an $\mathbb{R}^{N_x \times N_y \times N_z}$ tensor, since non-overlapping basis functions are used, as

$$\underline{\mathbf{G}}^{pl}(\mathbf{m}) = \int_{V_m} (N_m^l)^2 dV = \begin{cases} \Delta V & l = 1 \\ \frac{\Delta V}{12} & l = 2, 3, 4 \end{cases}, \quad (32)$$

where $\Delta V = \Delta x \Delta y \Delta z$ is the volume of the voxel.

Finally, the most challenging part in the assembly of the tensors is the calculation of the 6-D integrals that arise from the associated, discretized integro-differential \mathcal{N} and \mathcal{K} operators with kernels that exhibit strongly singular and weakly singular behavior, respectively, when the observation points coincide or are adjacent with the source points. More specifically, these integrals, according to (24) can be written as

$$\underline{\mathbf{N}}_{\mathbf{m},\mathbf{n}}^{pl,ql'} = \int_{V_m} \int_{V'_n} \mathbf{f}_m^{pl}(\mathbf{r}) \cdot \nabla \times \nabla \times (g(\mathbf{r} - \mathbf{r}') \mathbf{f}_n^{ql'}(\mathbf{r}')) dV' dV, \quad (33a)$$

$$\underline{\mathbf{K}}_{\mathbf{m},\mathbf{n}}^{pl,ql'} = \int_{V_m} \int_{V'_n} \mathbf{f}_m^{pl}(\mathbf{r}) \cdot \nabla \times (g(\mathbf{r} - \mathbf{r}') \mathbf{f}_n^{ql'}(\mathbf{r}')) dV' dV. \quad (33b)$$

The far interactions are calculated by means of a standard 6-D quadrature rule, where the components of the dyadic Green function kernels are symmetric and anti-symmetric for \mathcal{N} and \mathcal{K} operator, respectively, resulting in 6 and 3 unique dyadic components. Also, the unique interactions of the scalar part of the basis and testing functions with a kernel of the form $K(\mathbf{r}, \mathbf{r}') = K(\mathbf{r} - \mathbf{r}')$ are 10 instead of 16 interactions, when discretized on a uniform grid. These internal symmetries significantly reduce the overall memory footprint required for storing the tensors of both operators to 90 unique entries. However, simple quadrature rules cannot be applied when calculating the nearby interactions, since for coinciding or adjacent voxels the 6-D integrals are singular. The main idea for tackling these cases is to reduce the dimensionality of the volume-volume integrals to surface-surface step-by-step, as it has been shown in [33], [36]. As a result, the initial volume-volume integral boils down to a sum of 4 surface-surface integrals, over the faces of the interacting voxels, which have smoother kernels and can be calculated by modern algorithms, originally developed for Galerkin SIE methods over quadrilateral patches [43], [45].

In this work, we choose to use a uniform, voxelized grid which enables us to exploit the translation invariance property of the convolutional discrete kernels:

$$\underline{\mathbf{N}}_{\mathbf{m},\mathbf{n}}^{pl,ql'} = \underline{\mathbf{N}}_{\mathbf{m}-\mathbf{n}}^{pl,ql'}, \quad (34)$$

which means that we can fix the basis function at a specific voxel, say the first with $\mathbf{n} = (1, 1, 1)$, and sweep the testing function over the voxels of the computation domain in order to calculate only the unique volume-volume integrals. So, the above tensors $\in \mathbb{C}^{N_x \times N_y \times N_z \times N'_x \times N'_y \times N'_z}$, when expressed in matrix $\in \mathbb{C}^{N_V \times N_V}$ format will be three-level block-Toeplitz Toeplitz-block matrices, since we are dealing with the 3-D case. As a result, it suffices to calculate the Toeplitz defining tensors $\in \mathbb{C}^{N_x \times N_y \times N_z}$, as

$$\underline{\mathbf{N}}^{pl,ql'}(\mathbf{m}) = \underline{\mathbf{N}}_{\mathbf{m}-\mathbf{1}}^{pl,ql'}, \quad (35)$$

where $m_x = 1 : N_x$, $m_y = 1 : N_y$, $m_z = 1 : N_z$, $p, q \in \{x, y, z\}$ and $l, l' \in \{1, 2, 3, 4\}$. The same logic applies to the tensors for \mathcal{K} operator. Finally, even greater compression can be achieved by applying low multilinear rank tensor decompositions on the Toeplitz defining tensors [49]–[51].

IV. FFT-BASED VIE SOLVER

A. Acceleration of the Matrix-Vector Product

In order to numerically solve a discretized volume integral equation, the inversion of a very large and dense matrix is required. Hence, the scientific community has naturally

been using iterative solvers. However, even with an iterative solver, for which the most time consuming part is the matrix-vector product with $\mathcal{O}(N^2)$ complexity, solving a realistic problem becomes extremely difficult and in many cases prohibitive. However, if uniform, voxelized grids are used, the MoM matrix becomes structured (block Toeplitz with Toeplitz blocks) and the associated matrix-vector product is amenable to acceleration with the help of FFT resulting in $\mathcal{O}(N \log(N))$ complexity for each matrix vector product.

The first step to that direction is the embedding of the Toeplitz defining tensors for \mathcal{N} and \mathcal{K} operators into their respective circulant defining tensors $\underline{\mathbf{N}}_{\text{circ}}^{pl,ql'} \in \mathbb{C}^{2N_x \times 2N_y \times 2N_z}$, with special care to take into account the associated projection signs for the dyadic Greens functions, the basis, and testing functions, as described in a detailed algorithmic analysis, that can be found at the Appendix of [2], which we omit here for brevity. Finally, the circulant matrix-vector product can be computed with the FFT, reducing the computational cost to approximately $\mathcal{O}(N \log(N))$.

B. On Preconditioning

Furthermore, an advantage of using the current-based formulation is that the multiplicative operator with the dielectric susceptibilities is on the left of \mathcal{N} operator, as it can be seen in (15). Therefore, by multiplying through by the inverse of \mathcal{M}_{ϵ_r} , this equation can be rewritten as

$$(\mathcal{I} - \mathcal{M}_{\tau_e} \mathcal{N}) \mathbf{j} = c_e \mathcal{M}_{\tau_e} \mathbf{e}_{\text{inc}}, \quad (36)$$

with $\tau_e \triangleq \chi_e / \epsilon_r$, where the identity operator is now left alone. In this way, the integral equation is regularized and this regularization can be thought as a natural preconditioning for solving the linear system of the discretized current-based VIE, as it has been suggested in [55], [56]. Motivated from these observations, we use a preconditioner of the form $\mathbf{P} = \mathbf{M}_{\epsilon_r} \mathbf{G}$. From a numerical perspective, when using this preconditioner, the iterative solver converges much faster especially in the case of highly inhomogeneous scatterers. Numerical experiments, presented below, indicate the superior convergence properties of the iterative solver when using this preconditioned solver for the case of a RHBm.

C. Computation of Fields and Power

The linear system solution provides us with the equivalent electric and magnetic currents at the center of the voxels and the three linear coefficients represent the slopes of the linear terms. However, these quantities are mathematical inventions and do not represent any physical phenomenon or quantity. In this subsection, we describe the required steps for the computation of the EM fields and the associated absorbed power.

A fast and efficient way to calculate these quantities is by employing the fast matrix-vector products and calculating the "tested" total fields according to the discrete analogue of (16). Furthermore, it should be noted that, in order to calculate the fields in a discrete sense, we need to divide the "tested" fields by the Gram matrix. Finally, an advantage of this approach is that no extra memory is required for computing the fields,

and the complexity is once again governed by the FFT-based matrix-vector product.

Finally, the absorbed power can be accurately computed based on [52], where stable and compact vector-matrix-vector formulas are suggested. The only difference here is that we have to replace the Gram matrix, as in (32), to include the contributions of the linear terms of the solution vector and compute the absorbed power, which corresponds also to the SAR, as

$$P_{\text{abs}} = \frac{1}{2} \text{Re} \{ \mathbf{x}^* (c_e \mathbf{M}_{\chi_e})^{-1} \mathbf{G} \mathbf{x} \}, \quad (37)$$

with the $*$ superscript denoting the conjugate transpose operation.

V. NUMERICAL RESULTS

A. Solver Validation

To validate the proposed framework quantitatively, we conduct the numerical computation for the scattering of a plane wave from homogeneous dielectric spheres and calculate the absorbed power, as in (37). The results are compared with the Mie series solution [46]. In detail, we model frequency-dependent electrical properties, matched to the average of the gray and white matter according to [57], [58], as they can be seen in Table II, for various B_0 static magnetic field strengths of an MR scanner, where we use the gyromagnetic ratio as $\frac{\gamma}{2\pi} = 42.58 \text{ MHz/T}$ to set the operating frequency $f = \frac{\gamma}{2\pi} B_0$. Furthermore, the sphere has radius $r = 7.5 \text{ cm}$ and the excitation is an x -polarized and z -directed plane wave $\mathbf{e}_{\text{inc}} = \hat{\mathbf{x}} e^{-ik_0 z}$.

Moreover, we calculate the absorbed power, both with the PWC current-based VIE [2] and the proposed solver with PWL basis functions, and compute the relative error for the power obtained from Mie series, as $\text{error} = |\mathbf{P}_{\text{VIE}} - \mathbf{P}_{\text{Mie}}| / |\mathbf{P}_{\text{Mie}}|$. The iterative solver of choice is the Generalized Minimum Residual (GMRES) with inner iterations 50 and outer 200, and with tolerance 10^{-5} . Finally, we vary the resolution of the discretization, using $h = 5, 2.5, 1.5, 1$, and 0.75 mm , and present the results for the relative error of the PWC and PWL solvers, with respect to the resolution in Fig. 1, along with the Degrees of Freedom (DoFs) for each solver, shown in Table III. Clearly, the discretization with PWL basis functions gives much better accuracy with respect to the resolution, compared with the PWC discretization. Specifically, it is observed that there is a constant improvement factor of approximately 12 times in the relative error between the PWC and PWL solvers. However, the convergence rate appears to be $\mathcal{O}(h)$, instead of $\mathcal{O}(h^2)$, due to numerical inaccuracies originating from the staircase approximation of a sphere, when discretized with voxels.

B. Convergence Study for the Current-Based and Flux-Based Formulation

In this subsection, in order to demonstrate the superior convergence properties of the proposed high-order current-based solver, in comparison with the flux-based formulation [29], [30], often used in MRI studies [16], [59], we conduct

TABLE II
ELECTRICAL PROPERTIES

$B_0(\text{T})$	0.5	1.5	3	7
$f(\text{MHz})$	21.29	63.87	127.74	298.06
ϵ'_r	227	141	68	64
$\sigma(\text{S/m})$	0.25	0.35	0.5	0.51

TABLE III
DoFs

$h(\text{mm})$	5	2.5	1.5	1	0.75
$N_x = N_y = N_z$	31	61	101	151	201
DoFs PWC (million)	0.09	0.68	3.09	10.33	24.36
DoFs PWL (million)	0.36	2.72	12.36	41.32	97.45

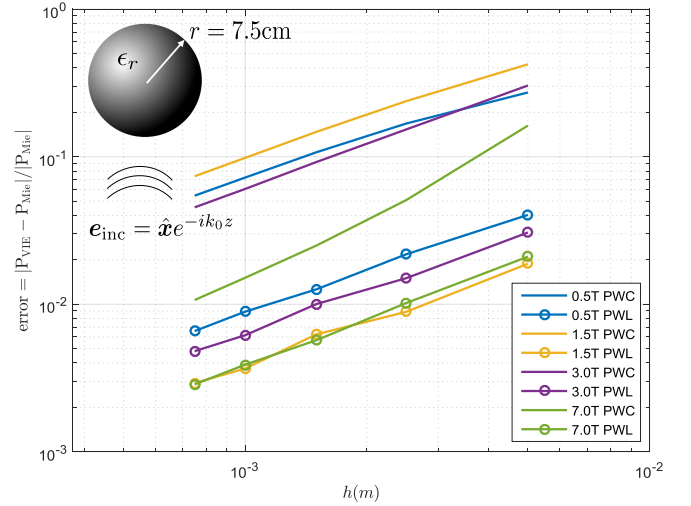


Fig. 1. Relative error of the absorbed power, with respect to the resolution, for the PWC and PWL current-based VIE, compared with the Mie series solution, for homogeneous spheres with $r = 7.5 \text{ cm}$ and frequency-dependent electrical properties, as in Table II, for each different B_0 , when irradiated by a plane wave.

the computations for the EM scattering of a plane wave for the "Billie" RHB from Virtual Family Population [47]. In detail, we operate at $B_0 = 7 \text{ T}$, hence the corresponding frequency is $f = 298.06 \text{ MHz}$ and we irradiate the RHB with an x -polarized and negative y -directed plane wave $\mathbf{e}_{\text{inc}} = \hat{\mathbf{x}} e^{ik_0 y}$, so that the plane wavefront is parallel to the coronal plane of the RHB.

Subsequently, we compute the EM fields and the absorbed power with the current-based formulation with PWC and PWL basis functions and the flux-based (DVIE) formulation with rooftop basis functions, as we refine the grid, using resolutions $h = 5, 2$, and 1 mm . Furthermore, GMRES is utilized with the same tolerance, inner and outer iterations as in the previous example. In Fig. 2, we present the root mean square (RMS) electric field at an axial cut for all 3 resolutions and 3 solvers, where the fields outside the body are masked for enhanced visualization. It is observed that, for

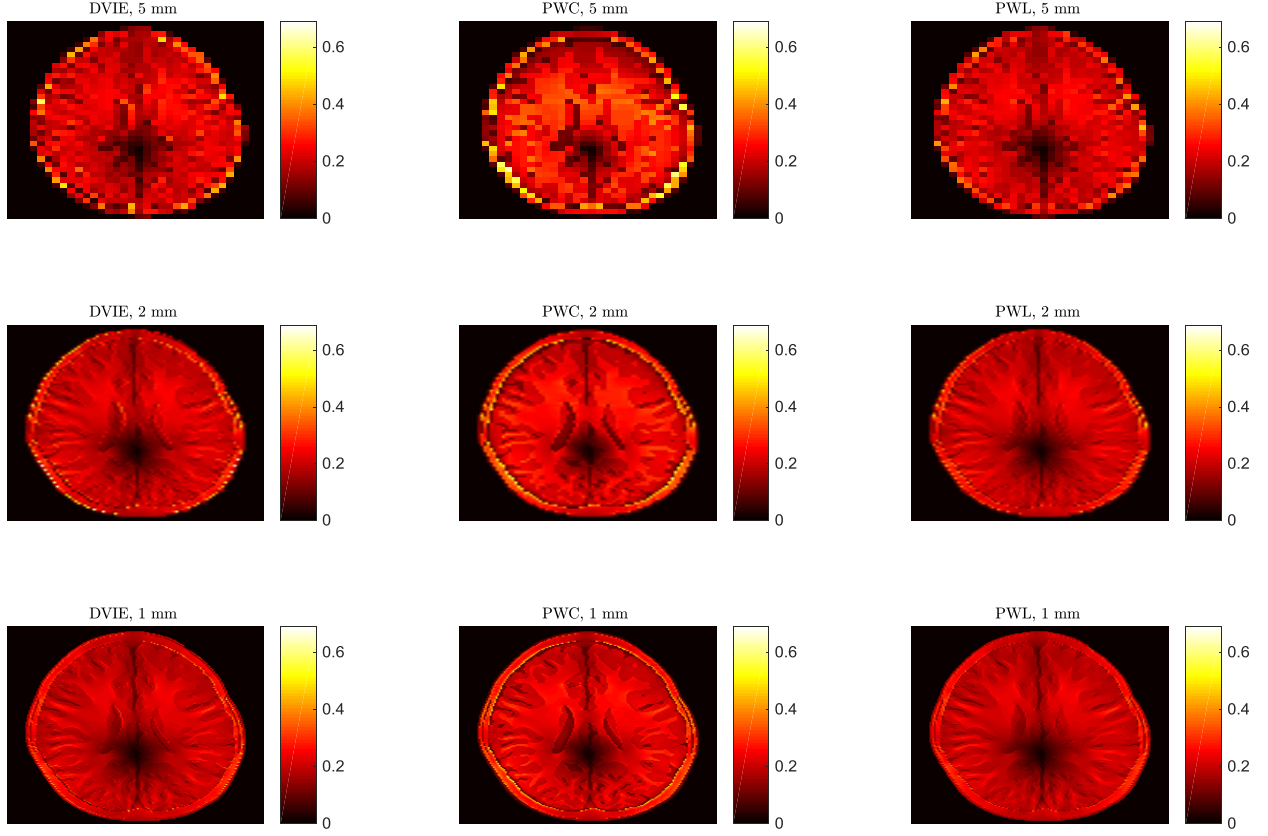


Fig. 2. Axial views of the root mean square (RMS) value of the electric field in the "Billie" RHBM, when excited by a plane wave at 7 T MRI. From left to right, the electric field values are obtained with the flux-based solver (DVIE), the PWC current-based solver, and the PWL current-based solver for resolutions $h = 5, 2$, and 1 mm, as viewed from top to bottom. Fields outside the body are masked to improve the visibility.

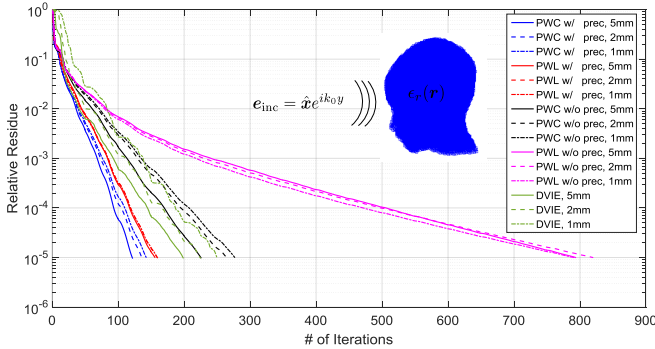


Fig. 3. Convergence of GMRES iterative solver for the PWC current-based solver, the PWL current-based solver with and without preconditioner, and the flux-based solver (DVIE) for different resolutions $h = 5, 2$, and 1 mm, for the calculation of the EM scattering of a plane wave from the "Billie" RHBM at 7 T MRI.

coarser resolutions, the PWL solver provides more accurate results, when compared with the lower-order PWC solver. Additionally, both for the case of DVIE and PWC solvers there exist numerical artifacts at regions with high contrast, i.e., at the air-skull and skull-brain interfaces, which is not the case for the proposed higher-order solver. Moreover, we execute the same numerical experiment, utilizing the preconditioner mentioned in the previous section, and present the convergence

of the iterative solver for all formulations and refinements.

As it can be clearly seen in Fig. 3, the current-based formulation is well-conditioned, allowing for p -refinement, while the iteration count remains practically the same, when the suggested preconditioner is used. It also allows for h -refinement, since, as we move to finer resolutions, the number of iterations does not change, which is not the case for the flux-based formulation, that diverges as we refine the grid. This can be attributed to the fact that the flux-based VIE, in [30], averages the normalized contrast function with the material properties and due to the fact that this formulation is inherently ill-conditioned and the number of iterations increases with h -refinement, as it is demonstrated at [22], [24]. On the contrary, when discretizing the current-based VIE, the spectral properties of the operators are preserved. Finally, the effectiveness of the proposed preconditioner for highly inhomogeneous scatterers can be verified since the iteration count is dramatically reduced when it is utilized, especially for the case of the PWL solver.

C. Convergence Study for the Case of a High-Dielectric Pad Attached to the RHBM and Comparison with FDTD

As it is proposed at [60]–[69], the use of high permittivity dielectric materials can effectively address b_1^+ inhomogeneities that arise in high-field MRI, where the effective wavelength is comparable to the dimensions of the subject. By introducing

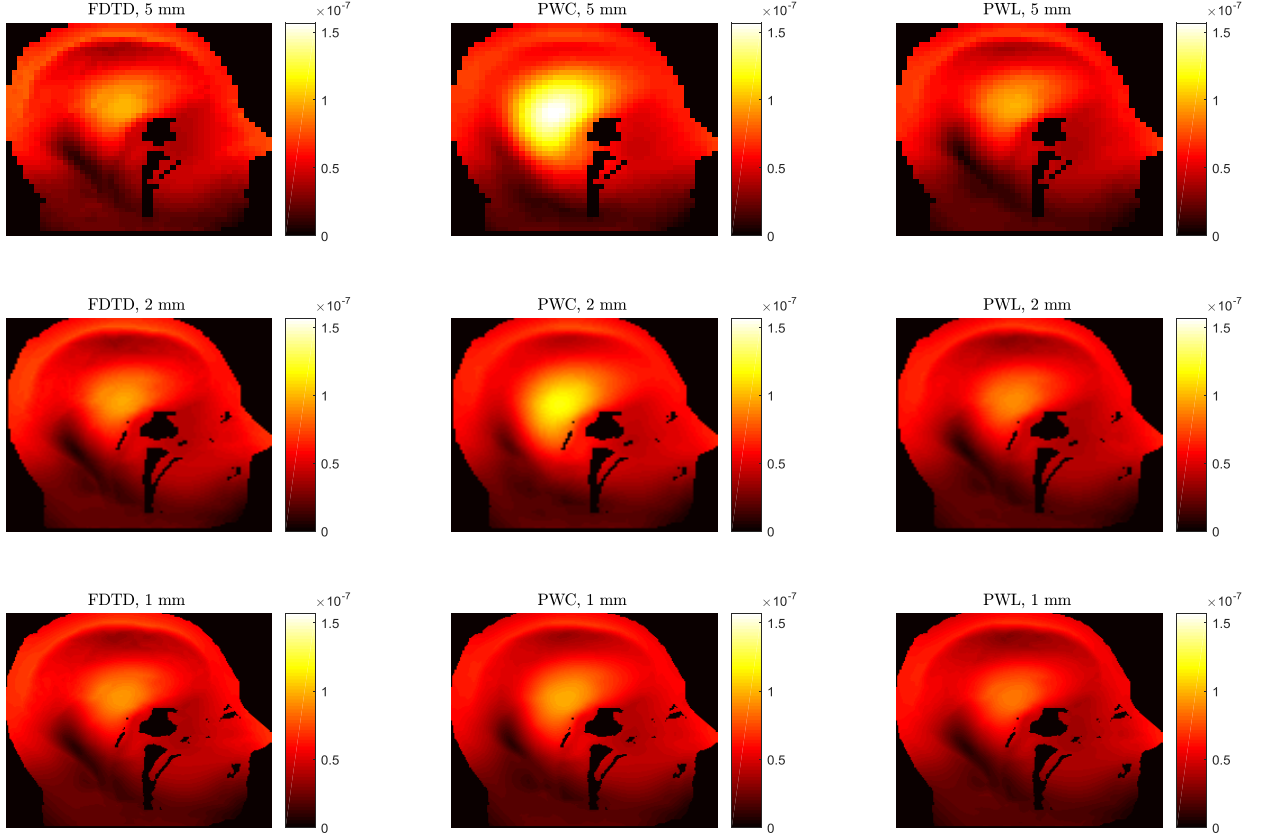


Fig. 4. Sagittal views of $|b_1^+|$ in the "Duke" RHB with an attached high-dielectric pad, when excited by a tuned birdcage coil at 7 T MRI. From left to right, the magnetic field values are obtained with a commercial FDTD package, the PWC current-based solver, and the PWL current-based solver for resolutions $h = 5, 2$, and 1 mm, as viewed from top to bottom. Fields outside the body and at the pad are masked to enhance the visibility.

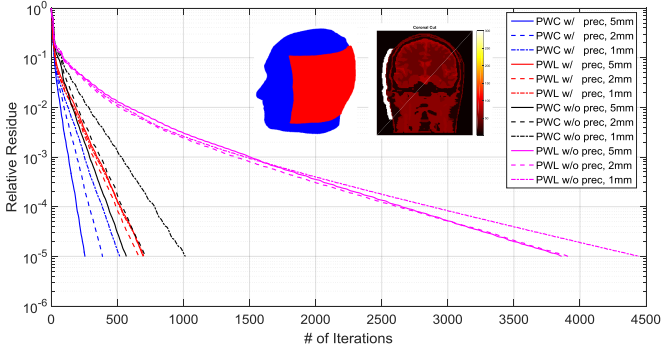


Fig. 5. Convergence of GMRES iterative solver for the PWC current-based solver and the PWL current-based solver with and without preconditioner for different resolutions $h = 5, 2$, and 1 mm, for the calculation of the EM scattering from the "Duke" RHB with an attached high-dielectric pad irradiated by a tuned birdcage coil at 7 T MRI. Also, the coronal view of the simulated geometry and the geometry of the attached pad are presented.

specifically designed dielectric pads between the RF coil and the subject, b_1^+ becomes more homogeneous, SAR is reduced and SNR increases, a technique called dielectric shimming. However, from an EM scattering perspective, simulating such setups is very challenging even for the state-of-the-art VIE-based solvers, due to the extremely high contrast and high

inhomogeneity of the scatterer.

To demonstrate the superior accuracy of the proposed current-based VIE solver with PWL basis functions, we perform the numerical computation for the EM scattering for the "Duke" RHB, where a highly dielectric pad is attached to the left side of the head of the model with dielectric properties of $\epsilon_r' = 300$ and $\sigma = 0.25$ S/m. The geometry and properties of the suspensions, as well as the incident field, which originates from a 16-rung high-pass birdcage coil with sinusoidal excitation tuned and matched at $f = 300$ MHz, are thoroughly explained in [65].

Subsequently, we calculate the EM field distributions over the head and the pad with the current-based VIE formulation with PWC and PWL basis functions, as we refine the resolution of the computational grid, using $h = 5, 2$, and 1 mm. Also, GMRES is utilized with the same tolerance, inner and outer iterations as before. The results are qualitatively compared to the EM fields obtained from a commercial software package which employs the finite difference time domain (FDTD) method (xFDTD 7.2, Remcom Inc., State College, Pennsylvania, USA), as it is mentioned at [65], and the $|b_1^+|$ at a sagittal cut for all 3 resolutions and 3 solvers is presented at Fig. 4, masking the fields outside the body for improved visibility. From that figure, it is clear that, even for this very demanding simulation, the PWL solver yields reliable and accurate EM fields for coarse resolutions, which are in

good agreement with the FDTD-based solution, despite the inherent differences in the numerical modeling of the setting. On the contrary, it is necessary to refine the resolution up to 1 mm for the PWC solver to converge to an accurate solution.

Finally, we execute the same numerical experiment for the PWC and PWL solvers utilizing the preconditioner mentioned in the previous section and present the convergence for the iterative solver for all the refinements at Fig. 5. Here, the well-conditioned properties of the current-based VIE can be observed, even for this extremely challenging scenario, allowing both for the utilization of higher-order approximations and grid refinements. Furthermore, the remarkable effectiveness of the proposed preconditioner is clearly demonstrated, since when it is utilized the number of iterations significantly drops from 3900 to 700, a value comparable to the iteration count of the PWC solver, allowing for this solver to be used in practical and demanding applications with manageable computational cost while simultaneously providing accurate and reliable results. Finally, it is worth noting that without the proposed preconditioner the iteration count of the PWL solver diverges at the finest resolution of 1 mm which does not occur when the preconditioner is employed.

VI. CONCLUSIONS

A fast VIE solver based on the equivalent polarization/magnetization currents with PWL basis functions is derived for the accurate computation of the EM scattering from highly inhomogeneous and/or high contrast objects. The proposed solver has remarkably stable convergence properties and yields reliable EM fields for extremely challenging modeling scenarios and for coarse resolutions without necessarily refining the computational grid. Furthermore, by discretizing the VIE on uniform grids, the matrix vector product can be performed fast with the help of FFT and, when combined with iterative solvers, large and complex problems can be solved accurately within reasonable time and computational resources. The proposed framework can be utilized in challenging applications such as the modeling of the interactions between EM fields and biological tissue, including the presence of shimming pads of very high electric permittivity.

ACKNOWLEDGMENT

The authors would like to thank Wyger M. Brink for providing the FDTD data, the geometry of the attached pad, and for useful discussions.

REFERENCES

- [1] J. F. Villena *et al.*, "Fast electromagnetic analysis of MRI transmit RF coils based on accelerated integral equation methods," *IEEE Transactions on Biomedical Engineering*, vol. 63, no. 11, pp. 2250–2261, 2016.
- [2] A. G. Polimeridis *et al.*, "Stable FFT-JVIE solvers for fast analysis of highly inhomogeneous dielectric objects," *Journal of Computational Physics*, vol. 269, pp. 280–296, 2014.
- [3] A. G. Polimeridis, J. F. Villena, and J. Seralles, "MARIE - MAGnetic Resonance Integral Equation suite, available online," 2015. [Online]. Available: <https://github.com/thanospol/MARIE>
- [4] C.-T. Tsai *et al.*, "A procedure for calculating fields inside arbitrarily shaped, inhomogeneous dielectric bodies using linear basis functions with the moment method," *IEEE transactions on microwave theory and techniques*, vol. 34, no. 11, pp. 1131–1139, 1986.
- [5] J. Markkanen and P. Ylä-Oijala, "Discretization of electric current volume integral equation with piecewise linear basis functions," *IEEE Transactions on Antennas and Propagation*, vol. 62, no. 9, pp. 4877–4880, 2014.
- [6] F. Wei and A. E. Yilmaz, "A 2-D decomposition based parallelization of AIM for 3-D BIOEM problems," in *Antennas and Propagation (APSURSI), 2011 IEEE International Symposium on*. IEEE, 2011, pp. 3158–3161.
- [7] G. Rubinacci and A. Tamburrino, "A broadband volume integral formulation based on edge-elements for full-wave analysis of lossy interconnects," *IEEE transactions on antennas and propagation*, vol. 54, no. 10, pp. 2977–2989, 2006.
- [8] C.-C. Lu, "A fast algorithm based on volume integral equation for analysis of arbitrarily shaped dielectric radomes," *IEEE transactions on antennas and propagation*, vol. 51, no. 3, pp. 606–612, 2003.
- [9] N. A. Ozdemir and J.-F. Lee, "A nonconformal volume integral equation for electromagnetic scattering from anisotropic materials," in *Antennas and Propagation Society International Symposium 2006, IEEE*. IEEE, 2006, pp. 2889–2892.
- [10] —, "A nonconformal volume integral equation for electromagnetic scattering from penetrable objects," *IEEE Transactions on Magnetics*, vol. 43, no. 4, pp. 1369–1372, 2007.
- [11] M. F. Catedra, E. Gago, and L. Nuno, "A numerical scheme to obtain the RCS of three-dimensional bodies of resonant size using the conjugate gradient method and the fast Fourier transform," *IEEE transactions on antennas and propagation*, vol. 37, no. 5, pp. 528–537, 1989.
- [12] H. Gan and W. C. Chew, "A discrete BCG-FFT algorithm for solving 3D inhomogeneous scatterer problems," *Journal of Electromagnetic Waves and Applications*, vol. 9, no. 10, pp. 1339–1357, 1995.
- [13] L. Sun and W. Chew, "A novel formulation of the volume integral equation for electromagnetic scattering," *Waves in Random and Complex Media*, vol. 19, no. 1, pp. 162–180, 2009.
- [14] M. Li and W. C. Chew, "Applying divergence-free condition in solving the volume integral equation," *Progress In Electromagnetics Research*, vol. 57, pp. 311–333, 2006.
- [15] W. C. Chew *et al.*, *Fast and efficient algorithms in computational electromagnetics*. Artech House, Inc., 2001.
- [16] J. Jin *et al.*, "Computation of electromagnetic fields for high-frequency magnetic resonance imaging applications," *Physics in medicine and biology*, vol. 41, no. 12, p. 2719, 1996.
- [17] M. Costabel, E. Darrigrand, and E. Koné, "Volume and surface integral equations for electromagnetic scattering by a dielectric body," *Journal of Computational and Applied Mathematics*, vol. 234, no. 6, pp. 1817–1825, 2010.
- [18] L.-M. Zhang and X.-Q. Sheng, "Discontinuous Galerkin volume integral equation solution of scattering from inhomogeneous dielectric objects by using the SWG basis function," *IEEE Transactions on Antennas and Propagation*, vol. 65, no. 3, pp. 1500–1504, 2017.
- [19] D. Borup and O. Gandhi, "Fast-Fourier-transform method for calculation of SAR distributions in finely discretized inhomogeneous models of biological bodies," *IEEE transactions on microwave theory and techniques*, vol. 32, no. 4, pp. 355–360, 1984.
- [20] C. S. Geyik *et al.*, "FDTD vs. AIM for bioelectromagnetic analysis," in *Antennas and Propagation Society International Symposium (APSURSI), 2012 IEEE*. IEEE, 2012, pp. 1–2.
- [21] J. Markkanen *et al.*, "Analysis of volume integral equation formulations for scattering by high-contrast penetrable objects," *IEEE Transactions on Antennas and Propagation*, vol. 60, no. 5, pp. 2367–2374, 2012.
- [22] J. Markkanen, P. Ylä-Oijala, and A. Sihvola, "Discretization of volume integral equation formulations for extremely anisotropic materials," *IEEE Transactions on Antennas and Propagation*, vol. 60, no. 11, pp. 5195–5202, 2012.
- [23] J. Markkanen, "Volume potential-integral-equation formulation for electromagnetic scattering by dielectric objects," in *Electromagnetic Theory (EMTS), 2016 URSI International Symposium on*. IEEE, 2016, pp. 468–471.
- [24] P. Ylä-Oijala *et al.*, "Surface and volume integral equation methods for time-harmonic solutions of Maxwell's equations," *Progress In Electromagnetics Research*, vol. 149, pp. 15–44, 2014.
- [25] S. Antenor de Carvalho and L. de Souza Mendes, "Scattering of EM waves by inhomogeneous dielectrics with the use of the method of moments and 3-D solenoidal basis functions," *Microwave and Optical Technology Letters*, vol. 23, no. 1, pp. 42–46, 1999.
- [26] D. Schaubert, D. Wilton, and A. Glisson, "A tetrahedral modeling method for electromagnetic scattering by arbitrarily shaped inhomogeneous dielectric bodies," *IEEE Transactions on Antennas and Propagation*, vol. 32, no. 1, pp. 77–85, 1984.

- [27] C. Y. Shen *et al.*, "The discrete Fourier transform method of solving differential-integral equations in scattering theory," *IEEE Transactions On Antennas and Propagation*, vol. 37, no. 8, pp. 1032–1041, 1989.
- [28] M. I. Sancer *et al.*, "On volume integral equations," *IEEE transactions on antennas and propagation*, vol. 54, no. 5, pp. 1488–1495, 2006.
- [29] P. Zwanborn and P. M. van den Berg, "A weak form of the conjugate gradient FFT method for plate problems," *IEEE Transactions on antennas and propagation*, vol. 39, no. 2, pp. 224–228, 1991.
- [30] P. Zwanborn and P. M. Van Den Berg, "The three dimensional weak form of the conjugate gradient FFT method for solving scattering problems," *IEEE Transactions on Microwave Theory and Techniques*, vol. 40, no. 9, pp. 1757–1766, 1992.
- [31] M. Van Beurden and S. Van Eijndhoven, "Gaps in present discretization schemes for domain integral equations," in *Electromagnetics in Advanced Applications, 2007. ICEAA 2007. International Conference on*. IEEE, 2007, pp. 673–675.
- [32] —, "Well-posedness of domain integral equations for a dielectric object in homogeneous background," *Journal of Engineering Mathematics*, vol. 62, no. 3, pp. 289–302, 2008.
- [33] I. P. Georgakis and A. G. Polimeridis, "Reduction of volume-volume integrals arising in Galerkin JM-VIE formulations to surface-surface integrals," in *Antennas and Propagation (EUCAP), 2017 11th European Conference on*. IEEE, 2017, pp. 324–326.
- [34] A. Polimeridis *et al.*, "Robust J-EFVIE solvers based on purely surface integrals," in *Electromagnetics in Advanced Applications (ICEAA), 2013 International Conference on*. IEEE, 2013, pp. 379–381.
- [35] E. H. Bleszynski, M. K. Bleszynski, and T. Jaroszewicz, "Reduction of volume integrals to nonsingular surface integrals for matrix elements of tensor and vector Green functions of Maxwell equations," *IEEE Transactions on Antennas and Propagation*, vol. 61, no. 7, pp. 3642–3647, 2013.
- [36] L. Knockaert, "On the analytic calculation of multiple integrals in electromagnetics," in *Electromagnetics in Advanced Applications (ICEAA), 2011 International Conference on*. IEEE, 2011, pp. 595–598.
- [37] A. G. Polimeridis and T. V. Yioultis, "On the direct evaluation of weakly singular integrals in Galerkin mixed potential integral equation formulations," *IEEE Transactions on Antennas and Propagation*, vol. 56, no. 9, pp. 3011–3019, 2008.
- [38] A. G. Polimeridis and J. R. Mosig, "Complete semi-analytical treatment of weakly singular integrals on planar triangles via the direct evaluation method," *International journal for numerical methods in engineering*, vol. 83, no. 12, pp. 1625–1650, 2010.
- [39] A. G. Polimeridis *et al.*, "Fast and accurate computation of hypersingular integrals in Galerkin surface integral equation formulations via the direct evaluation method," *IEEE transactions on antennas and propagation*, vol. 59, no. 6, pp. 2329–2340, 2011.
- [40] A. Polimeridis *et al.*, "On the evaluation of hyper-singular double normal derivative kernels in surface integral equation methods," *Engineering Analysis with Boundary Elements*, vol. 37, no. 2, pp. 205–210, 2013.
- [41] A. G. Polimeridis *et al.*, "DIRECTFN: Fully numerical algorithms for high precision computation of singular integrals in Galerkin SIE methods," *IEEE Transactions on Antennas and Propagation*, vol. 61, no. 6, pp. 3112–3122, 2013.
- [42] "DEMCEM package," 2016. [Online]. Available: <https://github.com/thanospol/DEMCEM>
- [43] "DIRECTFN package," 2016. [Online]. Available: <https://github.com/thanospol/DIRECTFN>
- [44] A. Tambova, G. Guryev, and A. G. Polimeridis, "On the fully numerical evaluation of singular integrals over coincident quadrilateral patches," in *Antennas and Propagation (EUCAP), 2017 11th European Conference on*. IEEE, 2017, pp. 3205–3208.
- [45] A. A. Tambova *et al.*, "On the generalization of DIRECTFN for singular integrals over quadrilateral patches," *IEEE Transactions on Antennas and Propagation*, vol. 66, no. 1, pp. 304–314, 2018.
- [46] G. Mie, "Beiträge zur optik trüber medien, speziell kolloidaler metal-lösungen," *Annalen der physik*, vol. 330, no. 3, pp. 377–445, 1908 (in german).
- [47] A. Christ *et al.*, "The Virtual Family-development of surface-based anatomical models of two adults and two children for dosimetric simulations," *Physics in medicine and biology*, vol. 55, no. 2, p. N23, 2009.
- [48] J. Van Gemert *et al.*, "An efficient methodology for the analysis of dielectric shimming materials in magnetic resonance imaging," *IEEE transactions on medical imaging*, vol. 36, no. 2, pp. 666–673, 2017.
- [49] A. G. Polimeridis and J. K. White, "On the compression of system tensors arising in FFT-VIE solvers," in *Antennas and Propagation Society International Symposium (APSURSI), 2014 IEEE*. IEEE, 2014, pp. 2144–2145.
- [50] I. I. Giannakopoulos, M. S. Litsarev, and A. G. Polimeridis, "3D cross-Tucker approximation in FFT-based volume integral equation methods," in *Antennas and Propagation Society International Symposium (APSURSI), 2018 IEEE*, 2018.
- [51] —, "Memory footprint reduction for the FFT-based volume integral equation method via tensor decompositions," *arXiv preprint arXiv:1811.00484*, 2018.
- [52] A. G. Polimeridis *et al.*, "On the computation of power in volume integral equation formulations," *IEEE Transactions on Antennas and Propagation*, vol. 63, no. 2, pp. 611–620, 2015.
- [53] J. Markkanen and P. Ylä-Oijala, "Numerical comparison of spectral properties of volume-integral-equation formulations," *Journal of Quantitative Spectroscopy and Radiative Transfer*, vol. 178, pp. 269–275, 2016.
- [54] G. C. Hsiao and R. E. Kleinman, "Mathematical foundations for error estimation in numerical solutions of integral equations in electromagnetics," *IEEE transactions on Antennas and Propagation*, vol. 45, no. 3, pp. 316–328, 1997.
- [55] G. P. Zouros and N. V. Budko, "Transverse electric scattering on inhomogeneous objects: Spectrum of integral operator and preconditioning," *SIAM Journal on Scientific Computing*, vol. 34, no. 3, pp. B226–B246, 2012.
- [56] N. V. Budko and A. B. Samokhin, "Spectrum of the volume integral operator of electromagnetic scattering," *SIAM Journal on Scientific Computing*, vol. 28, no. 2, pp. 682–700, 2006.
- [57] C. Gabriel, "Compilation of the dielectric properties of body tissues at RF and microwave frequencies." KING'S COLL LONDON (UNITED KINGDOM) DEPT OF PHYSICS, Tech. Rep., 1996.
- [58] B. Guérin *et al.*, "The ultimate signal-to-noise ratio in realistic body models," *Magnetic resonance in medicine*, vol. 78, no. 5, pp. 1969–1980, 2017.
- [59] S. Y. Huang *et al.*, "Fast full-wave calculation of electromagnetic fields based on weak-form volume integral equation for MRI applications," *The Journal of Engineering*, vol. 2018, no. 9, pp. 762–767, 2018.
- [60] A. Webb, "Dielectric materials in magnetic resonance," *Concepts in Magnetic Resonance Part A*, vol. 38A, no. 4, pp. 148–184, 2011.
- [61] P. de Heer *et al.*, "Increasing signal homogeneity and image quality in abdominal imaging at 3 T with very high permittivity materials," *Magnetic resonance in medicine*, vol. 68, no. 4, pp. 1317–1324, 2012.
- [62] W. M. Brink and A. G. Webb, "High permittivity pads reduce specific absorption rate, improve B1 homogeneity, and increase contrast-to-noise ratio for functional cardiac MRI at 3T," *Magnetic resonance in medicine*, vol. 71, no. 4, pp. 1632–1640, 2014.
- [63] W. M. Brink, J. S. van den Brink, and A. G. Webb, "The effect of high-permittivity pads on specific absorption rate in radiofrequency-shimmed dual-transmit cardiovascular magnetic resonance at 3T," *Journal of Cardiovascular Magnetic Resonance*, vol. 17, no. 1, p. 82, 2015.
- [64] R. Schmidt and A. Webb, "Improvements in RF shimming in high field MRI using high permittivity materials with low order pre-fractal geometries," *IEEE transactions on medical imaging*, vol. 35, no. 8, pp. 1837–1844, 2016.
- [65] W. M. Brink, R. F. Remis, and A. G. Webb, "A theoretical approach based on electromagnetic scattering for analysing dielectric shimming in high-field MRI," *Magnetic resonance in medicine*, vol. 75, no. 5, pp. 2185–2194, 2016.
- [66] K. Koolstra *et al.*, "Improved image quality and reduced power deposition in the spine at 3T using extremely high permittivity materials," *Magnetic resonance in medicine*, 2017.
- [67] G. G. Haemer *et al.*, "Approaching ultimate intrinsic specific absorption rate in radiofrequency shimming using high-permittivity materials at 7 tesla," *Magnetic resonance in medicine*, vol. 80, no. 1, pp. 391–399, 2018.
- [68] M. V. Vaidya *et al.*, "Manipulating transmit and receive sensitivities of radiofrequency surface coils using shielded and unshielded high-permittivity materials," *Magnetic Resonance Materials in Physics, Biology and Medicine*, pp. 1–12, 2018.
- [69] —, "Improved detection of fMRI activation in the cerebellum at 7T with dielectric pads extending the imaging region of a commercial head coil," *Journal of Magnetic Resonance Imaging*, 2018.